ACCOUNTS
of chemical research

Thermal and Nonthermal Physiochemical Processes in Nanoscale Films of Amorphous Solid Water

R. SCOTT SMITH,* NIKOLAY G. PETRIK,* GREG A. KIMMEL,* AND BRUCE D. KAY*

Fundamental and Computational Sciences Directorate, Pacific Northwest National Laboratory, P.O. Box 999, Mail Stop K8-88, Richland, Washington 99352, United States

RECEIVED ON MARCH 3, 2011

CONSPECTUS

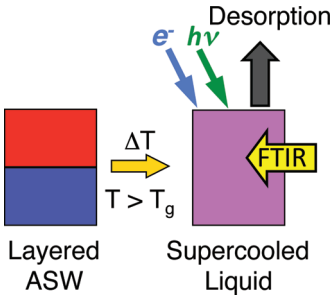

Amorphous solid water (ASW) is a disordered version of ice created by vapor deposition onto a cold substrate (typically less than 130 K). It has a higher free energy than the crystalline phase of ice, and when heated above its glass transition temperature, it transforms into a metastable supercooled liquid.

This unusual form of water exists on earth only in laboratories, after preparation with highly specialized equipment. It is thus fair to ask why there is any interest in studying such an esoteric material. Much of the scientific interest results from the ability to use ASW as a model system for exploring the physical and reactive properties of liquid water and aqueous solutions. ASW is also thought to be the predominant form of water in the extremely cold temperatures of many interstellar and planetary environments. In addition, ASW is a convenient model system for studying the stability of amorphous and glassy materials as well as the properties of highly porous materials. A fundamental understanding of such properties is invaluable in a diverse range of applications, including cryobiology, food science, pharmaceuticals, astrophysics, and nuclear waste storage, among others.

Over the past 15 years, we have used molecular beams and surface science techniques to probe the thermal and nonthermal properties of nanoscale films of ASW. In this Account, we present a survey of our research on the properties of ASW using this approach. We use molecular beams to precisely control the deposition conditions (flux, incident energy, and incident angle) and create compositionally tailored, nanoscale films of ASW at low temperatures. To study the transport properties (viscosity and diffusivity), we heat the amorphous films above their glass transition temperature, T_g, at which they transform into deeply supercooled liquids prior to crystallization. The advantage of this approach is that at temperatures near T_g, the viscosity is approximately 15 orders of magnitude larger than that of a normal liquid. As a result, the crystallization kinetics are dramatically slowed, increasing the time available for experiments. For example, near T_g, a water molecule moves less than the distance of a single molecule on a typical laboratory time scale (~1000 s). For this reason, nanoscale films help to probe the behavior and reactions of supercooled liquids at these low temperatures. ASW films can also be used for investigating the nonthermal reactions relevant to radiolysis.

I. Introduction

There exist several excellent reviews on the properties of amorphous solid water (ASW) and supercooled liquid water,[1−5] and a new comprehensive review is beyond the scope of this Account. Instead, we focus on our research over the past 15 years using molecular beams and surface science techniques to probe the thermal and nonthermal properties of nanoscale films of ASW. Through the use of

Published on the Web 05/31/2011 www.pubs.acs.org/accounts
10.1021/ar200070w

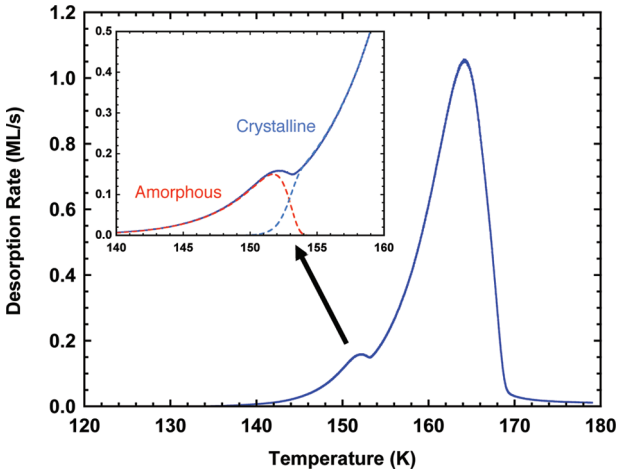

FIGURE 1. TPD spectrum from a 100 ML ASW film of H_2O deposited at normal incidence at 20 K on a Pt(111) substrate. The film was heated at 0.1 K/s. The inset shows an expanded view of the "bump" region showing the conversion from amorphous (red) to crystalline ice (blue).

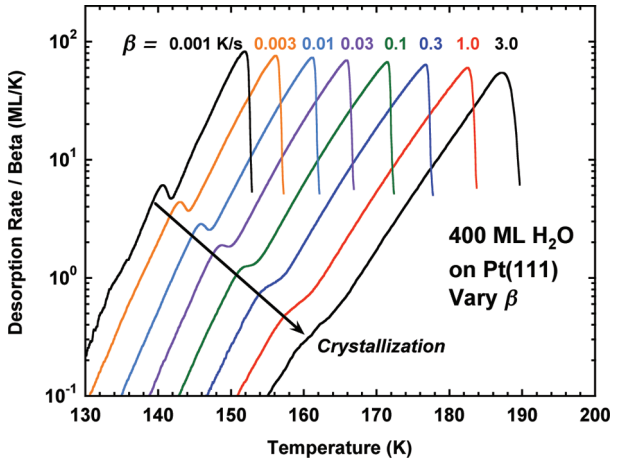

FIGURE 2. TPD spectra from 400 ML ASW films deposited at normal incidence and 20 K and then heated at various ramp rates. The spectra are plotted as the desorption rate (ML/s) divided by the ramp rate (K/s).

molecular beams, we can precisely control the deposition conditions (flux, incident energy, incident angle) to create compositionally tailored, nanoscale films of ASW at low temperatures. The use of nanoscale films allows us to probe the physical and chemical properties of ASW films at temperatures near where they transform into deeply supercooled liquids prior to crystallization. Amorphous materials are important in a wide range of scientific and technological areas[1−6] and an increased understanding of the properties of ASW may lead to a better understanding of amorphous materials in general. This Account is presented in two parts: section II, Thermal Properties of ASW, and section III, Nonthermal Reactions in ASW Films.

II. Thermal Properties of ASW

A. Desorption and Crystallization. The experiments were conducted in ultrahigh vacuum chambers using molecular beam and surface science techniques described elsewhere.[7] Amorphous solid water (ASW) is "trapped" in a structurally arrested or "frozen" disordered configuration that has a higher free energy than the stable crystalline configuration.[1−4] Hence, ASW has a higher vapor pressure (desorption rate) than the crystalline phase resulting in a "bump" in the desorption spectra of ASW films.[8−12] Figure 1 displays a typical ramped desorption spectrum. At low temperatures, desorption is from the amorphous solid, but as the film is heated, it transforms to the more stable crystalline phase. The inset displays the crystallization region where the dashed lines are kinetic model simulations showing desorption from the amorphous and crystalline phases.

It is important to note that the crystallization of ASW is not reversible and does not occur at a single temperature, like for example, melting or boiling, but instead is a kinetic phenomenon where the system irreversibly transforms to a stable crystalline state. Further, the temperature where the crystallization occurs depends on the experimental conditions. Figure 2 demonstrates that increasing the heating rate, β, shifts the crystallization from low to high temperature.[12] Note that with increased heating rates, the crystallization bump becomes less pronounced because the crystallization gets stretched out over a wider temperature range. Additionally, crystallization occurs at a smaller fraction of the film desorbed with increasing heating rate indicating that the activation energy for crystallization exceeds that of desorption.[12] The crystallization kinetics of ASW films can be determined from a fractional weighting of the desorption from the amorphous and crystalline phases.

Strictly speaking, the desorption kinetics and other surface-sensitive techniques such as inert gas physisorption,[13,14] only reveal information regarding of the outer surface of the film, while infrared spectroscopy probes the entire film, surface and bulk.[7,12] Figure 3a displays isothermal time-resolved spectra of the OH stretching region[15] for a 200 ML film. The first spectrum (red) in the series is from a completely amorphous film, and the last spectrum (blue) is from a completely crystallized film. The spectra intersect at an isosbestic point indicating that they can be analyzed as a linear combination of amorphous and crystalline phases. The vertical dashed line at 3307

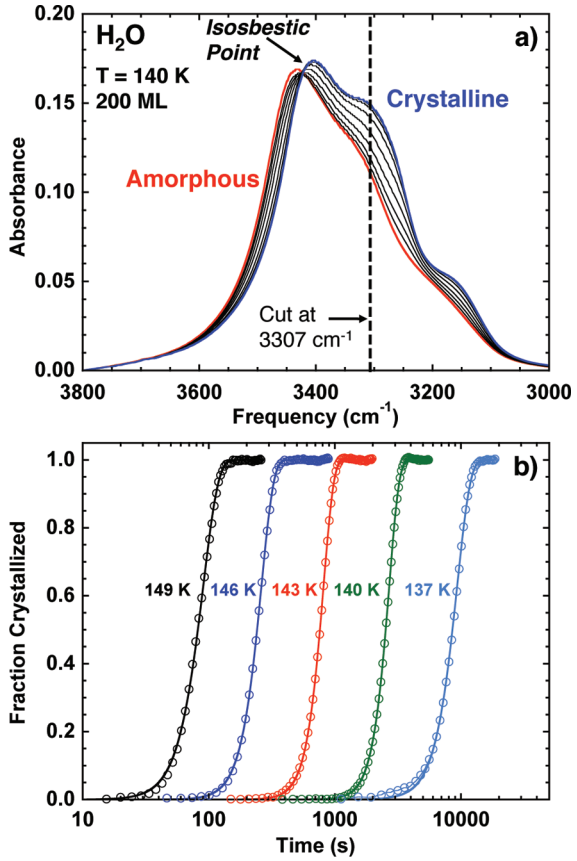

FIGURE 3. (a) Time-resolved infrared spectra of the OH stretch region of a 200 ML film. The first spectrum (red) is from a completely amorphous film, and the last spectrum (blue) is from a crystallized film. The isosbestic point indicates that the spectra in between are undergoing crystallization. The vertical dashed line at 3307 cm^{-1} is a cut used to analyze the fraction crystallized versus time. (b) The fraction crystallized versus time for a series of 200 ML films (symbols) held at several isothermal temperatures.

cm^{-1} is a cut through the time series of spectra that was used to analyze the fraction crystallized versus time.

Figure 3b displays the fraction crystallized (symbols) versus time obtained from data sets analogous to those in Figure 3a. The time to crystallize increases with decreasing temperature. Furthermore, each of the individual curves has the sigmoidal shape characteristic of nucleation and multidimensional growth kinetics. The lines are fits using the Avrami equation, $x(t) = 1 - \exp(-(kt)^n)$, where t is time, k is the phenomenological rate constant, and n is related to the crystallization mechanism. For all temperatures, the fit values of n were near 4, indicating spatially random nucleation and isotropic three-dimensional growth.[12] The value of k is a convolution of both the nucleation and growth rates. Details regarding the independent nucleation and growth rates have been published previously using more detailed kinetic models.[16]

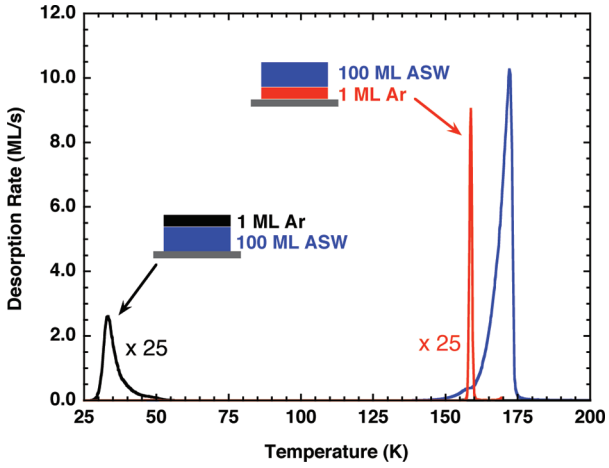

FIGURE 4. TPD spectra for 1 ML of Ar deposited on top (black) and underneath (red) of 100 ML ASW (blue) films.

Crystallization rates determined from both infrared and desorption experiments are in good agreement.[12]

Crystallization of ASW can result in structural changes in the film.[10,17] Figure 4 displays temperature-programmed desorption (TPD) spectra for 1 ML of Ar deposited on top and underneath a 100 ML ASW film. When deposited on top, the Ar desorbs below 50 K, however when deposited underneath, Ar remains trapped under the film until crystallization. We have termed the episodic release of trapped gases from ASW the "molecular volcano".[10,17] The observed abrupt desorption is likely due to the formation of cracks, fissures, or grain boundaries that accompany the crystallization kinetics and form a connected release pathway. Such microstructural evolution may be important in astrophysical ices. For example, comets often release trapped gases when heated. The extent to which ices can trap and retain gases can be important in determining the chemical composition of astrophysical bodies.[18,19]

B. Free Energy and Diffusivity. There has been a long-standing question as to whether there is continuity between the liquid melt of ASW and supercooled liquid water.[1−4] The question arises because many thermodynamic properties of supercooled liquid water appear to diverge at temperatures well above the reported glass transition for water.[2,4,9] The desorption rates from the amorphous and crystalline phases can be used to determine the excess free energy and entropy of ASW near 150 K,[9,12] since the desorption rate is directly related to the vapor pressure when the sticking coefficient of water is unity.[20,21] The free-energy difference between the amorphous and crystalline phases is given by $\Delta G = RT \ln(\text{rate}_{\text{amorphous}}/\text{rate}_{\text{crystalline}})$.

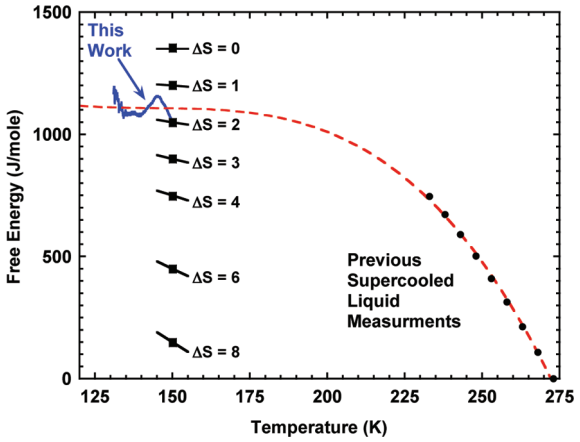

FIGURE 5. The experimental excess free energy for ASW (blue line) calculated from the ASW and crystalline desorption rates and for supercooled liquid H_2O (circles) from the literature.[23]

Arguments have suggested that for there to be thermodynamic continuity, the excess free energy of the melt of ASW near 150 K must be greater than its value at 236 K.[22,23] A problem for continuity arises because the calorimetrically measured enthalpy (ΔH(150 K) = 1350 J/mol) and theoretical estimates of the entropy (ΔS(150 K) = 6−9 J/(mol K)) predict free energies that are less than the value at 236 K.[24] Figure 5 displays the H_2O excess free energy (blue line) calculated using the desorption rate data (not shown) along with experimental values of the free energy of supercooled liquid water that extend to ∼236 K (circles).[12] From these data, we estimate the free energy to be 1100 ± 50 kJ/mol and the entropy to be 1.6 ± 1 J/(mol K) at temperatures near 150 K. The calculated free energies at 150 K (squares) are displayed in Figure 5 for various values of ΔS. The plot shows that for thermodynamic continuity, the excess free energy must be greater than ∼740 J/mol, and the excess entropy must be less than ∼4 J/(mol K). Our measured excess free energy and entropy meet these criteria and thus are consistent with thermodynamic continuity (dashed line) between ASW and supercooled liquid water. Note that the excess entropy for ASW (1−2 kJ/(mol K)) is much smaller than the entropy difference between liquid water and crystalline ice at 0 °C (22 kJ/(mol K)). Similarly, the enthalpy of crystallization at 150 K (∼1.35 kJ/mol) is also much smaller than the heat of crystallization of liquid water (∼6 kJ/mol). These relatively small values indicate that the structure of ASW is rather similar to crystalline ice, that is, the ASW structure likely consists of a high degree of coordination via intermolecular hydrogen bonding.

Another question is whether the transport properties of ASW just above its T_g can be connected to those of normal

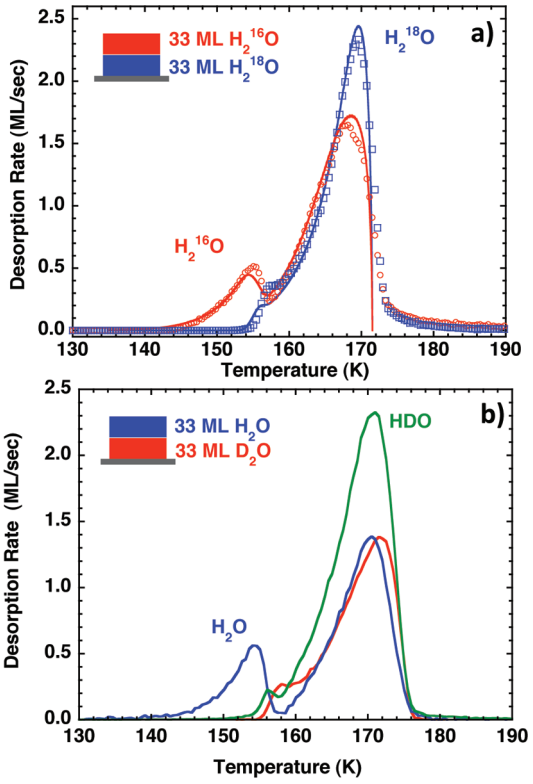

FIGURE 6. (a) TPD spectra from a composite film with 33 ML of $H_2{}^{16}O$ (○) on top of 33 ML of $H_2{}^{18}O$ (□). The lines are simulations using a one-dimensional diffusive transport model. (b) TPD spectra from a composite film of 33 ML of H_2O on top of 33 ML of D_2O.

liquid water. To explore this question, composite layers of isotopically labeled ASW were created. The initially unmixed film was then heated, and the diffusivity of the ASW melt was determined by the extent of isotopic intermixing between the composite layers.[11,25,26] Figure 6a displays a typical experiment where $H_2{}^{16}O$ layers were deposited on top of $H_2{}^{18}O$. Initially, desorption is observed only from the top species ($H_2{}^{16}O$), but at temperatures near the crystallization bump, desorption is observed from both species indicating intermixing of the isotopically labeled layers. Similarly in Figure 6b, isotopic layers of H_2O and D_2O show analogous behavior with the product yield of HDO being consistent with complete intermixing and rapid isotopic exchange in concert with the translational motion.[11,25,26]

Simulations (lines in Figure 6a) using a kinetic model that couples desorption, crystallization, and diffusion are in good agreement with the experimental results.[11,25,26] The extracted diffusivities range from ∼1 × 10^{-15} cm^2/s at 150 K to ∼1 × 10^{-12} cm^2/s near 160 K. These values can be connected with the diffusivities of liquid and supercooled liquid using a Vogel−Fulcher−Tamman (VFT) equation suggesting that ASW exhibits liquid-like translational diffusion

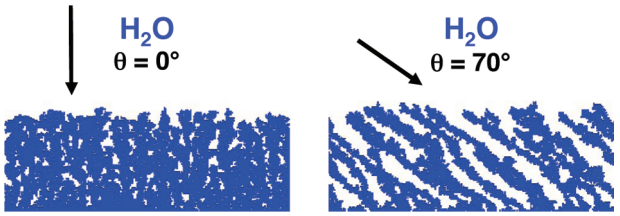

FIGURE 7. Ballistic deposition model simulations for the growth of ASW films at incident growth angles of 0° (left) and 70° (right).

that is consistent with the idea that ASW melts into a deeply supercooled metastable extension of normal liquid water (albeit a very viscous liquid) prior to crystallization.[11,25,26] Others have recently studied diffusion in ASW using a similar approach and have shown that the intermixing is heating rate dependent.[27] These recent findings[27] suggest that the diffusion kinetics are more complicated than indicated in our earlier studies[11,25,26] and vapor transport along cracks may play an important role. Additional experiments are needed to completely resolve this question.

C. Morphology of ASW. The morphology of ASW films depends on many factors including impingement flux, impingement energy, and substrate temperature. We have shown that the morphology of ASW films grown by vapor deposition also depends on the incident growth angle of water molecules from the gas phase.[7,28−31] By increasing the angle of incidence of the impinging molecules, one can grow films with structures from nonporous to highly porous. A simple physical mechanism, ballistic deposition, can be used to understand the dependence of morphology on the growth angle, which is illustrated in Figure 7.[7,28−32] At normal incidence (left panel), an incoming particle sees a nearly unobstructed path to the surface creating a relatively dense, nonporous film. At glancing angles (right panel), however, random height differences that arise during the initial film growth can block incoming flux. This essentially creates shadows that result in void regions in the shadows. If surface or bulk diffusion are slow compared with the incident flux, that is, the molecules "hit and stick", then the voids remain unfilled. Continued deposition results in porous films with filamentous columnar morphologies.

Figure 8 displays the relative intensity of the dangling OH stretch and the saturation uptake of nitrogen versus incident angle for 100 ML ASW films.[7] At normal and near-normal incident angles, no or very little porosity develops in the films. At higher incident angles (greater than ∼30°), the dangling bond intensity and nitrogen uptake increases revealing the onset of porosity. The dangling bond intensity continues to increase up to 85°, whereas the nitrogen

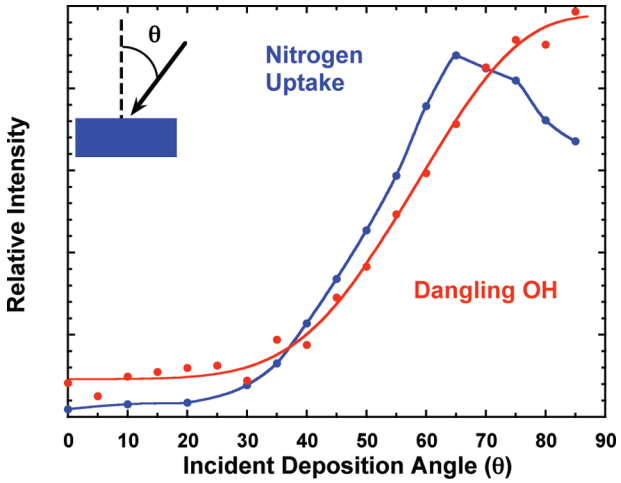

FIGURE 8. Nitrogen uptake (blue) and dangling OH bond intensity (red) for 100 ML ASW films deposited at various deposition angles.

uptake has a maximum at ∼65°. The explanation for this is that the dangling bond intensity and nitrogen uptake techniques are measuring different physical quantities: surface area for the dangling bond and surface area and pore condensation in the case of nitrogen physisorption. The reason for the maximum in the nitrogen uptake experiments is because the nitrogen uptake consists of two components: nitrogen adsorbed directly on the ASW surface and nitrogen condensed into pores. At large incident deposition angles, the pore radii become larger, which lowers the pore vapor pressure due to a larger radius of curvature (an inverse Kelvin effect). This results in less nitrogen being condensed at higher incident angles.[7,29,30]

Because the shadowing model is based on the assumption that incoming molecules will "hit-and-stick", other factors such as the incident collision energy[7,29,30] and substrate temperature will also affect the porosity of vapor-deposited films. Note that water films grown by background deposition at temperatures below ∼100 K, a common laboratory practice, will have porosities similar to films grown at glancing incident angles (60−80°). ASW is a major component in astrophysical ices and its morphology will affect the adsorption, desorption, trapping, and release of volatile gas species, such as H_2, CO, CO_2, CH_4, and hydrocarbons, which are believed to be components of these ices.[18,19]

III. Nonthermal Reactions in ASW Films

Energetic processes at surfaces and interfaces are important in fields such as photocatalysis, radiation chemistry, waste processing, and advanced materials synthesis. As a result, a detailed understanding of the nonthermal reactions occurring at interfaces is highly desirable. Low-energy excitations

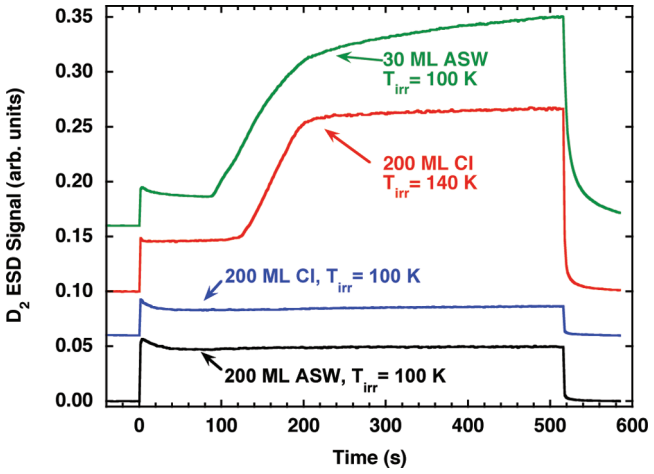

FIGURE 9. D_2 electron-stimulated desorption (ESD) signals at 100 or 140 K vs time from CI and ASW D_2O films adsorbed on Pt(111). Incident electron energy is 87 eV.[34] The electron beam is turned on at $t = 0$ s and turned off at $t = 520$ s.

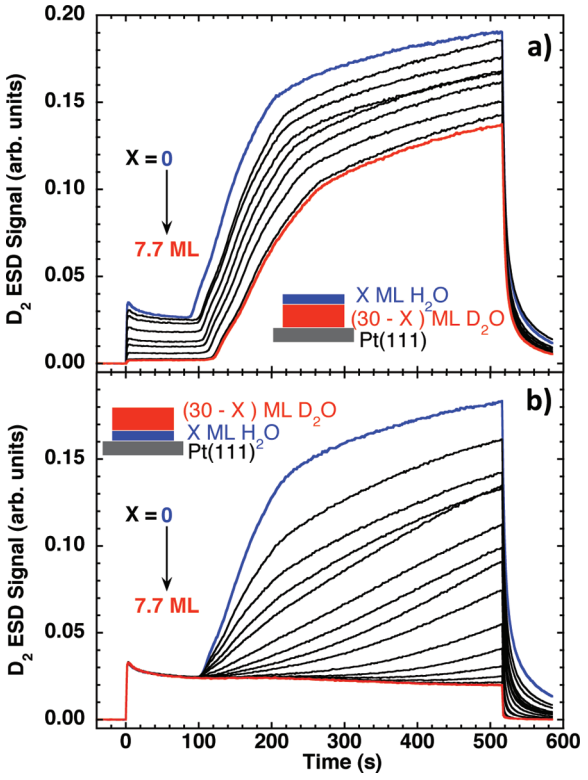

FIGURE 10. D_2 ESD signals vs time from isotopically layered ASW films of D_2O and H_2O. The films were deposited at 120 K and irradiated at 100 K with 87 eV electrons: (a) $(30 - X)$ ML D_2O capped with X ML of H_2O, where X changes from 0 (top curve) to 7.7 ML (bottom curve). Incident electron energy is 87 eV. (b) $(30 - X)$ ML D_2O deposited on top of an X ML H_2O spacer, where X changes from 0 (top) to 7.9 ML (bottom curve).[34]

frequently play a dominant role in the energetic processes. For example, the interaction of high-energy radiation with molecular solids results in the production of numerous, chemically active, secondary electrons with energies that are typically less than ~100 eV. Since the penetration depth of low-energy electrons in condensed phases is typically a few nanometers or less, they are well-suited for studying reactions that are localized at an interface.

In many systems, nonthermal reactions occur at aqueous interfaces, and thus the structure of the water at the interface plays an important role. Because the structure of water is perturbed at interfaces, it is expected that the thermal and nonthermal reactivity at the interfaces can be different than in the bulk. These factors provide our motivation for studying the low-energy, electron-stimulated reactions occurring in thin ASW films adsorbed on substrates such as Pt(111) and TiO_2(110).[33−40] Our experiments are conducted in ultrahigh vacuum (~1×10^{-10} Torr) on clean, well-characterized single crystals.[34] Thin water films are deposited using a molecular beam, then irradiated with a beam of monoenergetic, low-energy electrons that is rastered over the entire water film. Desorbing species such as water, H_2, and O_2 are detected with a quadrupole mass spectrometer. For the experiments reported here, the results depend on the electron fluence but are independent of the electron flux. As described below, experiments using isotopically layered water films show that the electron-stimulated reactions occur mostly at the ASW/substrate and ASW/vacuum interfaces and not in the bulk. However, the *energy* for the reactions is absorbed in the bulk of the films and is transferred to the interfaces via mobile electronic excitations. The energy migrates through the hydrogen-bonded water network over relatively large distances (tens to hundreds of monolayers in some cases). Developing a detailed understanding of these surprising phenomena remains a topic of ongoing investigation.

When ASW and crystalline ice films are irradiated with low-energy electrons, molecular hydrogen and molecular oxygen are two of the primary reaction products. For example, Figure 9 shows the D_2 electron-stimulated desorption (ESD) signal versus time from several D_2O films that were deposited on Pt(111) and irradiated with 87 eV electrons.[41] For a 30 ML amorphous D_2O film (Figure 9, green line), the D_2 ESD signal demonstrates two distinct kinetic components: The D_2 ESD increases promptly when the electron beam is turned on and subsequently increases again after ~90 s.[33,34] The reaction rates for each component depend on several factors including the phase of the water (ASW vs crystalline ice (CI)), the irradiation temperature, and the incident electron energy. For example, only the prompt kinetic component (which is nearly independent of electron fluence) is

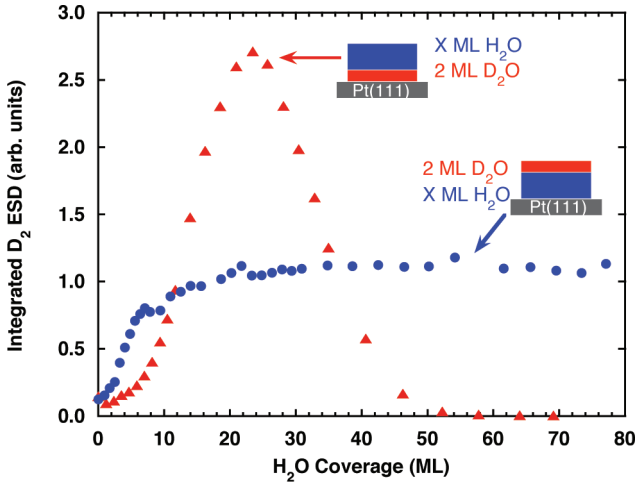

FIGURE 11. Integrated D_2 ESD yields vs H_2O coverage from isotopically layered ASW films of 2 ML D_2O and various coverages of H_2O. Incident electron energy is 87 eV.[34]

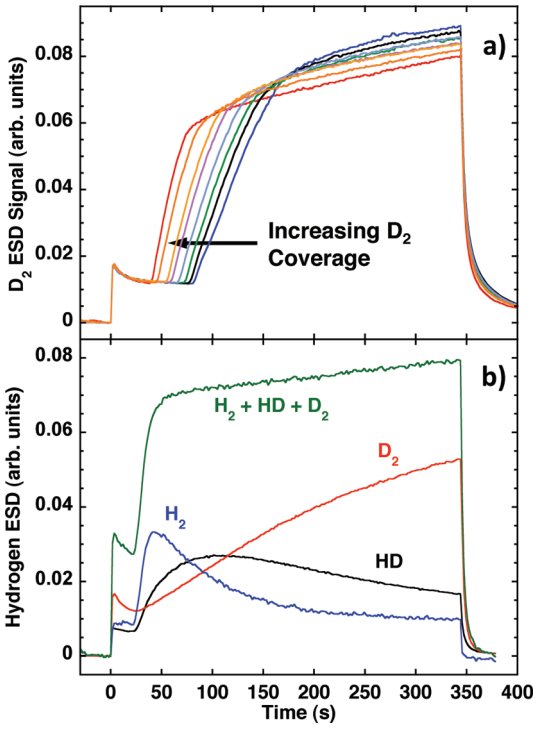

FIGURE 12. D_2, HD, and H_2 ESD yields versus time for 30 ML D_2O films adsorbed on Pt(111) predosed with (a) deuterium atoms or (b) hydrogen atoms.

seen for 200 ML ASW and CI films irradiated at 100 K (Figure 9, black and blue lines). On the other hand, for a 200 ML CI film irradiated at 140 K, the dose-dependent second component appears after ~145 s (Figure 9, red line).

Experiments with layered films of D_2O and H_2O show that the two kinetic components seen in the D_2 ESD versus time (Figure 9) are associated with reactions in different regions of the ASW films.[33,34] For example, Figure 10 shows the D_2 ESD versus time for various layered films of D_2O and H_2O, where the total amount of water, $\theta_{tot} = \theta_{D_2O} + \theta_{H_2O}$, is constant at 30 ML. In Figure 10a, a H_2O "cap layer" is deposited on top of the D_2O, and in Figure 10b, a H_2O "spacer layer" is first deposited on the Pt(111) before the D_2O is added. As the H_2O cap layer coverage is increased, the prompt initial increase in the D_2 ESD is suppressed (Figure 10a), while the dose-dependent component appearing at later times is largely unchanged. This result indicates that the prompt D_2 ESD, D_2(vac), is associated with reactions at the vacuum interface. For the H_2O spacer layer (Figure 10b), D_2(vac) is unchanged, but the dose-dependent component of the D_2 ESD is rapidly suppressed as θ_{H_2O} increases. This indicates that the dose-dependent component, D_2(Pt), is associated with reactions at the ASW/Pt interface. The integrated ESD yields for D_2(Pt) and D_2(vac) versus θ_{H_2O} decay exponentially with $1/e$ constants of 1 and 2.7 ML, respectively, showing that these reactions are localized at the interfaces of the ASW films (data not shown).[34]

The results in Figure 10 indicate that the majority of the molecular hydrogen is produced at the interfaces of the ASW film. However, another set of experiments demonstrates that the energy that initiates these reactions is not necessarily deposited where the reactions occur. Figure 11 shows the integrated D_2(Pt) ESD yield from 2 ML of D_2O deposited on Pt(111) and subsequently capped with H_2O versus θ_{H_2O} (triangles). Surprisingly, *for a fixed amount of D_2O*, D_2(Pt) increases rapidly as the H_2O coverage increases until $\theta_{H_2O} \approx 23$ ML (a ~25-fold increase!). At higher coverages, the D_2(Pt) signal decreases, but D_2 ESD is measurable for even thicker films (e.g., $\theta_{H_2O} = 100$ ML) after longer irradiation times or for experiments done at higher temperatures. Conversely, if 2 ML of D_2O is deposited on top of a H_2O spacer layer, D_2(vac) increases monotonically as θ_{H_2O} increases and saturates for $\theta_{H_2O} > 30$ ML (Figure 11, circles). The integrated D_2(vac) yield for thick films is ~9 times larger than yield of 2 ML of D_2O adsorbed directly on the Pt(111).

The results in Figure 11 clearly demonstrate that energy, which is deposited in the ASW film by the incident electrons, migrates to the interfaces where it drives the reactions that lead to the production of molecular hydrogen. Since 87 eV incident electrons penetrate into the water film less than ~20 ML,[42] the energy must be transported through the film over relatively long distances. Earlier ESD experiments on velocity distributions of D,[43] O, and D_2 and the rotational state distributions of D_2[44] also provided evidence for the

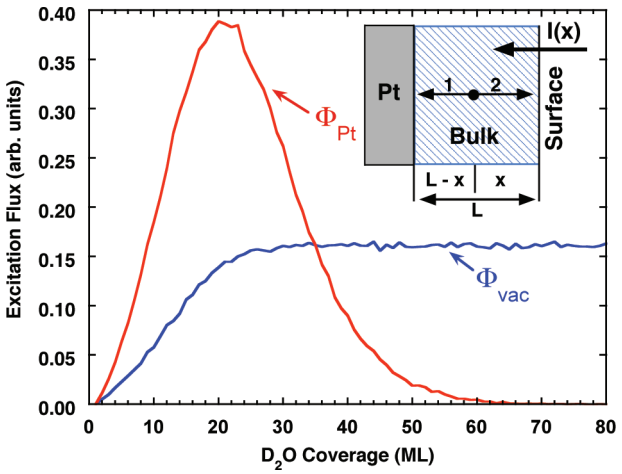

FIGURE 13. Random walk model results for the flux of excitations reaching the ASW/vacuum (Φ_{vac}) and ASW/Pt (Φ_{Pt}) interfaces versus film thickness. The inset shows a model schematic. Excitations are produced with a probability distribution $I(x)$ within water films of thickness L.

rapid migration of energy, but not atoms or molecules, from the bulk of the film to the ASW/vacuum interface.

Several experiments provide insight into the D_2 production at the ASW/Pt interface. For example, post-irradiation water TPD spectra show that deuterium atoms accumulate on the Pt(111) surface during electron irradiation of D_2O films (data not shown).[45] Once the deuterium coverage, θ_D, approaches saturation, reactions between adsorbed D lead to D_2 production. The irradiation time needed for θ_D to increase leads to the delayed production of D_2(Pt) seen in Figures 9 and 10. Therefore, increasing θ_D prior to adsorbing and irradiating a D_2O film should reduce the time required for D_2 to be produced at the ASW/Pt interface. Figure 12a shows an example where the substrate was exposed to increasing amounts of D_2, which dissociatively adsorbs on Pt(111), prior to depositing and irradiating a 30 ML D_2O film. For larger initial deuterium coverages, the induction period for D_2(Pt) production decreases. In Figure 12b, the surface was initially exposed to H_2 before adsorbing and irradiating a 30 ML D_2O film. Electron-stimulated reactions in the D_2O lead to D accumulation on the surface. However since the coverage of hydrogen is initially large, the reactions initially produce primarily H_2. As the reactions proceed, the hydrogen is depleted, θ_D increases, and the D_2 production eventually dominates. (D_2 produced at the vacuum interface is responsible for the prompt D_2 ESD signal and contributes an approximately constant signal throughout the irradiation, see Figure 10b.)

The results suggest that excitations in the ASW films migrate to the interfaces where they initiate reactions. Experiments indicate that D_2(vac) is proportional to the flux of excitations reaching the vacuum interface, and after the induction period, D_2(Pt) is proportional to the flux of excitations reaching the ASW/Pt interface (data not shown). A simple model allowing diffusion of an excitation from the bulk of the film to either interface qualitatively accounts for the results.[33] For a film of thickness L, excitations are produced with a distribution, $I(x)$, that is largest near the vacuum interface due to the limited penetration depth, L_e, of ~100 eV electrons. In the model, the excitations then undergo a random walk until they reach an interface, at which point they react. For an excitation at x (where $x = 0$ corresponds to the vacuum interface, Figure 13, inset), the probabilities of reaching the vacuum interface and substrate are $(1 - x)/L$ and x/L, respectively. Figure 13 shows the flux of excitations reaching the ASW/Pt and ASW/vacuum interfaces (Φ_{Pt} and Φ_{vac}, respectively), in one such model. For $L \ll L_e$, few excitations are produced, and thus little hydrogen is produced at either interface. For $L \gg L_e$, the flux of excitations reaching the substrate is small, and few reactions occur there. In contrast for $L \sim L_e$, excitations are produced, and they are likely to reach the substrate leading to a maximum in Φ_{Pt}. In this model, a higher reaction probability at the ASW/Pt interface is needed to account for the larger yield of D_2 from the ASW/Pt interface as compared with the ASW/vacuum interface (see Figure 11).

The experiments and model suggest that mobile electronic excitations are responsible for the reactions at the interfaces of thin ASW films. Protonic defects (e.g., H_3O^+), delocalized electrons,[46] holes,[47] and excitons[43,48,49] are potential candidates for the mobile excitations. Since reactions at the water/Pt interface can occur for thick water films (e.g., Figure 9), only relatively long-lived electronic excitations are likely to be involved. This would seem to argue against excitons, since the lowest electronically excited states of water are purely dissociative in the gas phase.[50] However, cluster calculations indicate that the lowest excited states of hydrogen-bonded water molecules are nondissociative.[50] This may inhibit exciton dissociation in the bulk in favor of dissociation at the interfaces. The excited state lifetimes may also be long enough to allow for exciton migration, which would provide a mechanism for energy transport in condensed water phases.[51] Furthermore, exciton diffusion to the interfaces of Ar films results in Ar desorption (i.e., sputtering), and the sputtering yield versus film thickness is qualitatively similar to the coverage dependence of the D_2 ESD yield due to reactions at the vacuum interface.[52] However, other mechanisms, such as hydrogen

transport to the substrate via the hopping of H_3O^+, may also be important, and more research is needed to firmly establish the mechanisms by which energy reaches the interfaces of these thin ASW films.

IV. Summary

In this Account, we have provided a brief survey of our work using ASW as a model to probe the thermal and nonthermal properties of water and amorphous materials. A key feature of the work is the use of molecular beams to synthesize compositionally tailored nanoscale films of various isotopes of water. More detail is available in the cited references. Future work will use ASW films as a model "solvent" to explore the physical and reaction properties of aqueous supercooled liquid solutions.

BIOGRAPHICAL INFORMATION

R. Scott Smith received his B.S. (1983) at Northern Arizona University and Ph.D. at the University of Utah (1988), both in chemistry. He has been a staff member at PNNL since 1992.

Nikolay Petrik received his Ph.D. in 1980 and Doctor of Sciences degree in 1994 (both in Chemistry) from the Institute of Technology, St. Petersburg, Russia. He is currently a Senior Research Scientist at PNNL. His interests are in surface and interfacial chemistry, radiation, and photochemistry.

Greg A. Kimmel received his B.S. in Engineering Physics (1984) and his Ph.D. in Applied Physics (1992) from Cornell University. He has been a staff member at PNNL since 1995. His research interests include thermal and nonthermal reactions at surfaces and interfaces, the structure and reactivity of thin water films, and photochemistry.

Bruce D. Kay received a B.S. in Chemistry from the University of Illinois (1976) and a Ph.D. in Chemical Physics from the University of Colorado (1982). From 1982 to 1991, he was on the technical staff at Sandia National Laboratory and joined PNNL as Laboratory Fellow in November 1991.

This work was supported by the U.S. Department of Energy (DOE), Office of Basic Energy Sciences, Division of Chemical Sciences, Geosciences, and Biosciences. The research was performed using EMSL, a national scientific user facility sponsored by DOE's Office of Biological and Environmental Research and located at Pacific Northwest National Laboratory, which is operated by Battelle for the U.S. DOE under Contract DE-AC05-76RL01830.

FOOTNOTES

*E-mail addresses: Scott.Smith@pnl.gov; Nikolai.Petrik@pnl.gov; Greg.Kimmel@pnl.gov; Bruce.Kay@pnl.gov.

REFERENCES

1 Angell, C. A. Amorphous Water. *Annu. Rev. Phys. Chem.* **2004**, *55*, 559–583.
2 Angell, C. A. Insights into Phases of Liquid Water from Study of Its Unusual Glass-Forming Properties. *Science* **2008**, *319*, 582–587.
3 Debenedetti, P. G. *Metastable Liquids: Concepts and Principles*; Princeton University Press: Princeton, NJ, 1996.
4 Debenedetti, P. G.; Stanley, H. E. Supercooled and Glassy Water. *Phys. Today* **2003**, *56*, 40–46.
5 Ediger, M. D.; Angell, C. A.; Nagel, S. R. Supercooled Liquids and Glasses. *J. Phys. Chem.* **1996**, *100*, 13200–13212.
6 Jenniskens, P.; Blake, D. F. Structural Transitions in Amorphous Water Ice and Astrophysical Implications. *Science* **1994**, *265*, 753–756.
7 Smith, R. S.; Zubkov, T.; Dohnalek, Z.; Kay, B. D. The Effect of the Incident Collision Energy on the Porosity of Vapor-Deposited Amorphous Solid Water Films. *J. Phys. Chem. B* **2009**, *113*, 4000–4007.
8 Smith, R. S.; Huang, C.; Wong, E. K. L.; Kay, B. D. Desorption and Crystallization Kinetics in Nanoscale Thin Films of Amorphous Water Ice. *Surf. Sci.* **1996**, *367*, L13–L18.
9 Speedy, R. J.; Debenedetti, P. G.; Smith, R. S.; Huang, C.; Kay, B. D. The Evaporation Rate, Free Energy, and Entropy of Amorphous Water at 150 K. *J. Chem. Phys.* **1996**, *105*, 240–244.
10 Smith, R. S.; Huang, C.; Wong, E. K. L.; Kay, B. D. The Molecular Volcano: Abrupt CCl_4 Desorption Driven by the Crystallization of Amorphous Solid Water. *Phys. Rev. Lett.* **1997**, *79*, 909–912.
11 Smith, R. S.; Kay, B. D. The Existence of Supercooled Liquid Water at 150 K. *Nature* **1999**, *398*, 788–791.
12 Smith, R. S.; Matthiesen, J.; Knox, J.; Kay, B. D. Crystallization Kinetics and Excess Free Energy of H_2O and D_2O Nanoscale Films of Amorphous Solid Water. *J. Phys. Chem. A* **2011**, 10.1021/jp110297q.
13 Dohnalek, Z.; Kimmel, G. A.; Ciolli, R. L.; Stevenson, K. P.; Smith, R. S.; Kay, B. D. The Effect of the Underlying Substrate on the Crystallization Kinetics of Dense Amorphous Solid Water Films. *J. Chem. Phys.* **2000**, *112*, 5932–5941.
14 Backus, E. H. G.; Grecea, M. L.; Kleyn, A. W.; Bonn, M. Surface Crystallization of Amorphous Solid Water. *Phys. Rev. Lett.* **2004**, *92*, No. 236101.
15 Devlin, J. P. Structure, Spectra, and Mobility of Low-Pressure Ices: Ice I, Amorphous Solid Water, and Clathrate Hydrates at T < 150 K. *J. Geophys. Res., [Planets]* **2001**, *106*, 33333–33349.
16 Safarik, D. J.; Mullins, C. B. A New Methodology and Model for Characterization of Nucleation and Growth Kinetics in Solids. *J. Chem. Phys.* **2003**, *119*, 12510–12524.
17 Ayotte, P.; Smith, R. S.; Stevenson, K. P.; Dohnalek, Z.; Kimmel, G. A.; Kay, B. D. Effect of Porosity on the Adsorption, Desorption, Trapping, and Release of Volatile Gases by Amorphous Solid Water. *J. Geophys. Res., [Planets]* **2001**, *106*, 33387–33392.
18 Klinger, J. Extraterrestrial Ice. A Review. *J. Phys. Chem.* **1983**, *87*, 4209–4214.
19 Allamandola, L. J.; Bernstein, M. P.; Sandford, S. A.; Walker, R. L. Evolution of Interstellar Ices. *Space Sci. Rev.* **1999**, *90*, 219–232.
20 Batista, E. R.; Ayotte, P.; Bilic, A.; Kay, B. D.; Jonsson, H. What Determines the Sticking Probability of Water Molecules on Ice? *Phys. Rev. Lett.* **2005**, *95*, No. 223201.
21 Brown, D. E.; George, S. M.; Huang, C.; Wong, E. K. L.; Rider, K. B.; Smith, R. S.; Kay, B. D. H_2O Condensation Coefficient and Refractive Index for Vapor-Deposited Ice from Molecular Beam and Optical Interference Measurements. *J. Phys. Chem.* **1996**, *100*, 4988–4995.
22 Angell, C. A. Water-II Is a Strong Liquid. *J. Phys. Chem.* **1993**, *97*, 6339–6341.
23 Speedy, R. J. Evidence for a New Phase of Water - Water-II. *J. Phys. Chem.* **1992**, *96*, 2322–2325.
24 Sceats, M. G.; Rice, S. A. The Entropy of Liquid Water from the Random Network Model. *J. Chem. Phys.* **1980**, *72*, 3260–3262.
25 Smith, R. S.; Huang, C.; Kay, B. D. Evidence for Molecular Translational Diffusion During the Crystallization of Amorphous Solid Water. *J. Phys. Chem. B* **1997**, *101*, 6123–6126.
26 Smith, R. S.; Dohnalek, Z.; Kimmel, G. A.; Stevenson, K. P.; Kay, B. D. The Self-Diffusivity of Amorphous Solid Water near 150 K. *Chem. Phys.* **2000**, *258*, 291–305.
27 McClure, S. M.; Barlow, E. T.; Akin, M. C.; Safarik, D. J.; Truskett, T. M.; Mullins, C. B. Transport in Amorphous Solid Water Films: Implications for Self-Diffusivity. *J. Phys. Chem. B* **2006**, *110*, 17987–17997.
28 Stevenson, K. P.; Kimmel, G. A.; Dohnalek, Z.; Smith, R. S.; Kay, B. D. Controlling the Morphology of Amorphous Solid Water. *Science* **1999**, *283*, 1505–1507.
29 Kimmel, G. A.; Dohnalek, Z.; Stevenson, K. P.; Smith, R. S.; Kay, B. D. Control of Amorphous Solid Water Morphology Using Molecular Beams. II. Ballistic Deposition Simulations. *J. Chem. Phys.* **2001**, *114*, 5295–5303.
30 Kimmel, G. A.; Stevenson, K. P.; Dohnalek, Z.; Smith, R. S.; Kay, B. D. Control of Amorphous Solid Water Morphology Using Molecular Beams. I. Experimental Results. *J. Chem. Phys.* **2001**, *114*, 5284–5294.
31 Dohnalek, Z.; Kimmel, G. A.; Ayotte, P.; Smith, R. S.; Kay, B. D. The Deposition Angle-Dependent Density of Amorphous Solid Water Films. *J. Chem. Phys.* **2003**, *118*, 364–372.
32 Barabasi, A. L.; Stanley, H. E. *Fractal Concepts in Surface Growth*; Cambridge University Press: Cambridge, U.K., 1995.

33 Petrik, N. G.; Kimmel, G. A. Electron-Stimulated Reactions at the Interfaces of Amorphous Solid Water Films Driven by Long-Range Energy Transfer from the Bulk. *Phys. Rev. Lett.* **2003**, *90*, No. 166102.

34 Petrik, N. G.; Kimmel, G. A. Electron-Stimulated Production of Molecular Hydrogen at the Interfaces of Amorphous Solid Water Films on Pt(111). *J. Chem. Phys.* **2004**, *121*, 3736–3744.

35 Petrik, N. G.; Kimmel, G. A. Electron-Stimulated Sputtering of Thin Amorphous Solid Water Films on Pt(111). *J. Chem. Phys.* **2005**, *123*, No. 054702.

36 Petrik, N. G.; Kavetsky, A. G.; Kimmel, G. A. Electron-Stimulated Production of Molecular Oxygen in Amorphous Solid Water on Pt(111): Precursor Transport through the Hydrogen Bonding Network. *J. Chem. Phys.* **2006**, *125*, No. 124702.

37 Petrik, N. G.; Kavetsky, A. G.; Kimmel, G. A. Electron-Stimulated Production of Molecular Oxygen in Amorphous Solid Water. *J. Phys. Chem. B* **2006**, *110*, 2723–2731.

38 Lane, C. D.; Petrik, N. G.; Orlando, T. M.; Kimmel, G. A. Site-Dependent Electron-Stimulated Reactions in Water Films on TiO_2(110). *J. Chem. Phys.* **2007**, *127*, No. 224706.

39 Lane, C. D.; Petrik, N. G.; Orlando, T. M.; Kimmel, G. A. Electron-Stimulated Oxidation of Thin Water Films Adsorbed on TiO_2(110). *J. Phys. Chem. C* **2007**, *111*, 16319–16329.

40 Petrik, N. G.; Kimmel, G. A. Nonthermal Water Splitting on Rutile TiO_2: Electron-Stimulated Production of H_2 and O_2 in Amorphous Solid Water Films on TiO_2(110). *J. Phys. Chem. C* **2009**, *113*, 4451–4460.

41 Qualitatively similar results are found for incident electron energies between ~20 and ~200 eV.

42 LaVerne, J. A.; Pimblott, S. M. Effect of Elastic Collisions on Energy Deposition by Electrons in Water. *J. Phys. Chem. A* **1997**, *101*, 4504–4510.

43 Orlando, T. M.; Kimmel, G. A. The Role of Excitons and Substrate Temperature in Low-Energy (5−50 Ev) Electron-Stimulated Dissociation of Amorphous D2O Ice. *Surf. Sci.* **1997**, *390*, 79–85.

44 Kimmel, G. A.; Tonkyn, R. G.; Orlando, T. M. Kinetic and Internal Energy-Distributions of Molecular-Hydrogen Produced from Amorphous Ice by Impact of 100 Ev Electrons. *Nucl. Instrum. Methods Phys. Res., Sect. B* **1995**, *101*, 179–183.

45 Petrik, N. G.; Kimmel, G. A. Electron-Stimulated Reactions in Thin D_2O Films on Pt(111) Mediated by Electron Trapping. *J. Chem. Phys.* **2004**, *121*, 3727–3735.

46 Bernas, A.; Ferradini, C.; JayGerin, J. P. On the Electronic Structure of Liquid Water: Facts and Reflections. *Chem. Phys.* **1997**, *222*, 151–160.

47 Souda, R. Bonding of Molecular Solids Probed by Low-Energy H+ Scattering. Water and Oxygen on Pt(111). *J. Phys. Chem. B* **2001**, *105*, 5–7.

48 Kobayashi, K. Optical-Spectra and Electronic-Structure of Ice. *J. Phys. Chem.* **1983**, *87*, 4317–4321.

49 Sukhonosov, V. Y. Formation of Excitons in Liquid Water During Irradiation. *High Energy Chem.* **1998**, *32*, 71–76.

50 Chipman, D. M. Excited Electronic States of Small Water Clusters. *J. Chem. Phys.* **2005**, *122*, 044111.

51 Chipman, D. M. Stretching of Hydrogen-Bonded OH in the Lowest Singlet Excited Electronic State of Water Dimer. *J. Chem. Phys.* **2006**, *124*, No. 044305.

52 Reimann, C. T.; Johnson, R. E.; Brown, W. L. Sputtering and Luminescence in Electronically Excited Solid Argon. *Phys. Rev. Lett.* **1984**, *53*, 600–603.